Contents lists available at ScienceDirect

Materials Science & Engineering A

Deformation induced twinning in hcp/bcc $Al_{10}Hf_{25}Nb_5Sc_{10}Ti_{25}Zr_{25}$ high entropy alloy – microstructure and mechanical properties

L. Rogal [a,*], U.D. Wdowik [b], M. Szczerba [a], N. Yurchenko [c], T. Czeppe [a], P. Bobrowski [a]

[a] Institute of Metallurgy and Materials Science, Polish Academy of Sciences, Reymonta 25, 30-059, Krakow, Poland
[b] Institute of Technology, Pedagogical University, Podchorazych 2, 30-084, Krakow, Poland
[c] Laboratory of Bulk Nanostructured Materials, Belgorod National Research University, Belgorod, 308015, Russia

ARTICLE INFO

ABSTRACT

High-entropy alloys of hexagonal structure commonly revealing high strength but very limited ductility, still remain a challenging task. Advanced strategy is proposed in present work in order to develop high-entropy alloy of chemical composition $Al_{10}Hf_{25}Nb_5Sc_{10}Ti_{25}Zr_{25}$ at.%. Crystallographic features and microstructures of as-cast and annealed $Al_{10}Hf_{25}Nb_5Sc_{10}Ti_{25}Zr_{25}$ at.% alloy are characterized by X-ray diffraction, scanning and high-resolution transmission electron microscopies, whereas differential scanning calorimetry is used to follow temperature-induced phase transformation in the as-cast system. The cast alloy reveals microstructure containing fine orthorhombic needle-like plates within solid-solution of body-centered cubic structure. Such a dual-phase microstructure leads to enhanced combination of high strength and good ductility. The alloy annealed at 1000 °C for 5h acquires tensile strength increased by 38%, yield strength more than ten times higher, and almost 3-fold increased plasticity as compared with the as-cast alloy. Its Vickers hardness becomes higher by 25%. These meaningful changes are associated with temperature-induced transformation of its microstructure, which include diffusion growth of hexagonal plates enriched in Zr, Sc, and Hf within the bcc-type matrix enriched in Nb and Ti. Microstructure reveals twins within the hcp plates which plays a crucial role in plastic deformation and strengthening of the materials. *Ab initio* calculations based on the density functional theory are employed to investigate stability and mechanical properties of bcc, hcp, and orthorhombic phases of 5-component $Al_{15}Hf_{25}Sc_{10}Ti_{25}Zr_{25}$ at.% and 6-component $Al_{10}Hf_{25}Nb_5Sc_{10}Ti_{25}Zr_{25}$ at.% high entropy alloys. The hcp phases of both systems are energetically preferred at T = 0 K, brittle and have rather high Vickers hardness. The bcc phases of both high-entropy alloys stabilize and become energetically favored above 790 K for $Al_{15}Hf_{25}Sc_{10-}Ti_{25}Zr_{25}$ at.% and 1150 K for $Al_{10}Hf_{25}Nb_5Sc_{10}Ti_{25}Zr_{25}$ at.% alloys. Depending on the type of crystallographic structure, the phases enriched in 5 at% of Nb show either reduced or enhanced values of their elastic moduli and Vickers hardness as compared to the Nb-free phases. No transformation from brittle to ductile state and vice versa is observed upon doping the considered phases of Al-Hf-Sc-Ti-Zr system with Nb.

1. Introduction

The design of new alloys by combining five or more elements with a typical content between 5 and 35 at.% — the class of high-entropy alloys (HEAs) — has stimulated interest of the scientific community due to the unique opportunity to develop engineering materials with superior properties [1–7]. In the early stages of HEA investigations, the vast majority of alloys belonged to the face-centered cubic (fcc) or body-centered cubic (bcc) solid solutions [1]. Since then, the class of HEAs has been extended and nowadays it includes also a number of hexagonal close packed (hcp) eutectic alloys of partially ordered structures as well as alloys containing secondary intermetallic phases [8–11]. The recently developed refractory complex concentrated alloys (RCCAs) (Senkov et al. [12]) are materials of a unique type and they consist of three or more principal refractory elements. They are characterized by a superior oxidation resistance and a relatively low density in comparison with other alloys [13–17]. Most of the HEA are single-phase fcc or bcc structures; however, these containing low-density elements, such as: Al, Ti, Zr, may also contain secondary phases. Among them, one may commonly observe ordered B2 or $L1_2$ as well as Laves intermetallic phases of poor ductility at room temperature [3,18]. Although some attempts were undertaken to develop

---

low-density HEA with a good combination of specific strength and ductility, these investigations have been limited to single-phase alloys. High-entropy alloys of the body-centered cubic structure have been reported to be ductile at room temperature [19–22]. Recently, the $Hf_{25}Sc_{25}Ti_{25}Zr_{25}$ alloy, which is a novel HEA with a single-phase hexagonal solid solution and needle-like structure has been designed [23]. The addition of Al to the Hf-Sc-Ti-Zr alloy leads to the formation of the $D0_{19}$ atomic order in the hexagonal lattice [24] and makes it an ideal starting point to explore a new subclass of alloys, but, on the other hand, the resulting alloy exhibits relatively low plasticity due to its ordered structure. In the present work it has been shown, that the optimized two-phase microstructure of HEA enriched by additional bcc solid solution reveals significantly increased plasticity, alike the two-phase Ti_6Al_4V alloys [5,25,26]. Motivated by the fact that the Al–Hf–Sc–Ti–Zr system displays structural morphology similar to that found in the titanium alloys, niobium was used as a β-phase stabilizing the alloying element. The addition of Nb results in an increase of ductility of the Ti_3Al-based alloys [27] and improves their oxidation resistance [5,25], strongly enhancing the formation of the bcc structure in the Ti_6Al_4Nb alloy, and stabilizing this phase at room temperature [25]. The Nb-enriched Ti–Al alloys reveal better strength, toughness, and creep resistance in comparison with single β-Ti systems [28,29]. The transformation induced plasticity (TRIP) has recently been observed in the $Ti_{35}Zr_{27.5}Hf_{27.5}Nb_5Ta_5$ HEA [30] due to the appearance of the metastable β-phase resulting in a superelastic effect in Ti–Zr–Hf–Al–Nb HEAs [28]. All these studies clearly indicate the high potential of Ti- and Nb-containing HEAs to reveal extraordinary properties. Therefore, following the recent studies on the $Al_{15}Hf_{25}Sc_{10}Ti_{25}Zr_{25}$ at.% HEA [24] we have enriched previously developed alloy with 5 at.% of Nb to obtain an advanced HE system which is expected to show the optimal combination of strength and ductility. The present experimental research addresses the impact of Nb content on the microstructure and mechanical properties of the Al-Hf-Sc-Ti-Zr high-entropy alloy and demonstrates that the formation of dual-phase structure in the $Al_{10}Hf_{25}Nb_5Sc_{10}Ti_{25}Zr_{25}$ at.% HEA leads to its superior properties over those found for the Nb-free alloy. The results of experimental studies are supported by *ab initio* calculations of the structural and mechanical properties of $Al_{15}Hf_{25}Sc_{10}Ti_{25}Zr_{25}$ at.% and $Al_{10}Hf_{25}Nb_5Sc_{10}Ti_{25}Zr_{25}$ at.% HEAs which are based on the density functional theory. Relying on the calculated temperature dependence of the Helmholtz free energies of the bcc, hcp, and orthorhombic phases of $Al_{15}Hf_{25}Sc_{10}Ti_{25}Zr_{25}$ at.% and $Al_{10}Hf_{25}Nb_5Sc_{10}Ti_{25}Zr_{25}$ at.% alloys the energetic stability of these phases is analyzed.

2. Methodology

2.1. Materials preparation

The $Al_{10}Hf_{25}Nb_5Sc_{10}Ti_{25}Zr_{25}$ at.% alloys were prepared from the elements of 99.99 wt% purity in an arc melting furnace with a water-cooled copper plate and under protective Ar atmosphere. The high purity titanium was applied as the getter. In the applied technology, the solidification proceeds at the average cooling rate of about 100 °C/s. To ensure sufficient homogenization, the alloys were re-melted 5 times. The samples of each batch were prepared with the target weight of 3.5 g and with the cylindrical shape of 10 mm in height and 10 mm in diameter. The overall chemical composition was 11.0% - Al, 23.5% - Hf, 6.4% – Nb, 9.1% - Sc, 25.1% - Ti, 24.9%- Zr (all in weight atomic pct). Some of ingots were also homogenized in a resistance furnace under Ar atmosphere at temperatures higher than 1000 °C for 5h.

2.2. Microstructural and mechanical properties analysis

In order to perform the structural characterization, the platelets were cut into 4 mm thick samples from the bottom of the cast. The phase composition was studied by the X-ray diffraction (XRD) and using a D2

Phaser-Bruker diffractometer with monochromatic CoK_α filtered radiation. The microstructure was examined using the scanning electron microscope FEI SEM XL30 (FEI Company, Hillsboro, OR) equipped with the energy-dispersive X-ray spectrometer EDAX GEMINI 4000 and the Tecnai G2 F20 transmission electron microscope (TEM). The micro-chemical analysis was conducted using TEM equipment in transmission and scanning transmission (STEM) modes coupled with the Integrated Energy-Dispersive X-ray spectroscopy (EDS). The samples for TEM were thinned with Struers Tenupol-5 jet polisher (Struers, Inc., Cleveland, OH) in the electrolyte consisting of 20 vol% $HClO_4$ and 80 vol% CH_3OH at subzero temperatures. The phase transformation was followed by the Netzsch DSC404F1 differential scanning calorimeter. The samples of 3 mm in diameter and 2 mm thick were heated in an alumina crucible at the rate of 15 °C min^{-1} up to 1500 °C in Ar atmosphere. The Vickers hardness was measured under the load of 5 kg using a Zwick/ZHU 250 tester. The average hardness was estimated based on 15 measurements. The results of tensile and compression strength tests were performed with the Instron 6025 testing machine at room temperature and the deformation rate of 10^{-3} 1/s. Tensile test experiments has been conducted to analysis mechanical properties. Micro-tensile test experiments have been conducted to analyze mechanical properties. First, the prepared alloy drops were cast into a cylindrical die with a diameter of 10 mm. Next, they were cut into discs with 2 mm thickness, and a symmetrical narrowing with the size of 2 mm was made, using an end mill (diameter: 3 mm). The compression test was performed on cylindrical samples that were 4 mm in diameter and 6 mm in height, following the PN-57/H-04320 standard. Three compression tests and three tensile tests were carried out for the studied alloys.

2.3. Computations

To represent random solid solutions of the 5-component $Al_{15}Hf_{25}Sc_{10}Ti_{25}Zr_{25}$ at.% and 6-component $Al_{10}Hf_{25}Nb_5Sc_{10}Ti_{25}Zr_{25}$ at.% high entropy alloys (HEAs) a supercell method was used along with a special quasi-random structures (SQS) approximation [31] to model their chemical disorder. Four phases of both, 5- and 6-component HEA, namely bcc A2, hcp A3, hcp $D0_{19}$, and orthorhombic A_{20} were investigated. Each phase was modeled by a 128-atom supercell, which contained 19 Al, 32 Hf, 12 Sc, 33 Ti, and 32 Zr atoms for 5-component HEA and 12 Al, 33 Hf, 6 Nb, 12 Sc, 33 Ti, and 32 Zr atoms for 6-component one. These supercells matched quite well the experimentally explored $Al_{15}Hf_{25}Sc_{10}Ti_{25}Zr_{25}$ at.% and $Al_{10}Hf_{25}Nb_5Sc_{10}Ti_{25}Zr_{25}$ at.% HEAs. The calculations were carried out within the framework of density functional theory (DFT) implemented in the VASP code [32,33]. The electron-ion interaction was represented by the projector augmented wave (PAW) method [34,35]. The generalized gradient approximation with parametrization of Perdew, Burke, and Ernzerhof (GGA-PBE) [36,37] was applied for the exchange and correlation potential. The wave functions were expanded in a plane-wave basis set with the cut-off energy of 360 eV. The PAW pseudopotentials with 3 valence electrons for Al and Sc, 4 valence electrons for Hf and Ti, 11 valence electrons for Nb, and 12 valence electrons for Zr were taken from the VASP database. Test calculations show that change in the number of valence electrons for Ti from 4 to 10 has rather marginal effect on the computed quantities. The structures were fully optimized with convergence criteria for the total energy and residual Hellman-Feynman forces of 10^{-6} eV and 10^{-2} eV/Å, respectively. The Brillouin zones of the bcc, hcp, and orthorhombic structures were sampled using, respectively, 32, 26, and 12 irreducible k-points generated according to the Monkhorst-Pack scheme. The single-crystal elastic constants of the bcc, hcp, and orthorhombic phases of $Al_{15}Hf_{25}Sc_{10}Ti_{25}Zr_{25}$ at.% and $Al_{10}Hf_{25}Nb_5Sc_{10}Ti_{25}Zr_{25}$ at.% HEAs were calculated according to the standard methodology [38] and then employed to determine the polycrystalline elastic moduli of these phases via the Voigt-Reuss-Hill averaging method [39,40]. Hardness of phase has been correlated with the phase elasticity using empirical formula proposed by Chen et al. [41]. This approximation has been shown to

give reasonable results for a wide variety of polycrystalline materials. The Vicker's hardness has been estimated as $H_V = 2 \, (k^2 \, G)^{0.585}$ - 3, where B (G) is the bulk (shear) modulus and k = G/B denotes the Pugh's ratio.

In order to investigate the evolution of phases, their relative energetic stability, and phase transformation as a function of temperature, the Helmholtz free energies of individual phases are calculated. For a given temperature, a stable phase is one for which the Helmholtz free energy has lowest value. The Helmholtz free energy of a given phase F (V,T) at volume V and temperature T is approximated as [40] $F(V,T) = E_0(V) + F_{vib}(V,T) + F_{el}(V,T) - TS_{conf}(T)$, where $E_0(V)$ is the energy of the rigid lattice obtained directly from *ab initio* calculations at 0 K, $F_{vib}(V,T)$ and $F_{el}(V,T)$ are the vibrational and thermal electronic contributions to the Helmholtz free energy, respectively. The $TS_{conf}(T)$ denotes term arising from the configurational entropy $S_{conf}(T)$, i.e., entropy of mixing. The $F_{vib}(V,T)$ is determined within the quasi-harmonic Debye-Grüneisen formalism [42,43] which takes into account anharmonic effects in quite simplified way, while the $F_{el}(V,T)$ is obtained under assumption of the temperature independent density of electron states [44,45]. Approximation of an ideal mixing is used to compute $S_{conf}(T)$ [46,47]. Details of calculating $F_{vib}(V,T)$, $F_{el}(V,T)$, and $TS_{conf}(T)$ contributions are provided and widely discussed in the pertinent literature [24,48–52].

3. Results and discussion

3.1. Characterization of the as-cast state

Fig. 1 shows the microstructure of the as-cast sample of $Al_{10}Hf_{25}Nb_5Sc_{10}Ti_{25}Zr_{25}$ at.% HEA, while the results of chemical analysis carried out with the EDS are summarized in Table 1. The light microscopy presented in Fig. 1a is taken in the direction perpendicular to the crystallization of the sample. It shows grains with average size up to 1 mm and a fine cellular dendritic microstructure inside. The SEM microstructure, which is displayed in Fig. 1b, reveals a dual-phase contrast inside the grains, which results from the differences in the chemical composition between cells and interdendritic volumes. The EDS chemical analysis from the brighter place (point 1 in Fig. 1, Table 1) and the darker area (point 2 in Fig. 1, Table 1) confirm the differences in the Al content of about 5 at.%. Additionally, dark points visible in the microstructure are identified as porosity. The analysis of these areas does not reveal any significant differences in the composition (point 3 in Fig. 1, Table 1). The X-ray diffraction spectra, presented in Fig. 2a and b demonstrate the presence of the body-centered cubic solid solution (space group *Im-3m*) with lattice parameter a = 3.448 Å and the secondary phase with the orthorhombic structure (space group: *Cmcm*) and lattice constants a = 3.034 Å, b = 5.34 Å, and c = 5.76 Å. The XRD results indicate that Nb addition stabilizes the bcc structure in the $Al_{10}Hf_{25}Nb_5Sc_{10}Ti_{25}Zr_{25}$ at.% HEA. The role of niobium was confirmed

Table 1
Results of SEM-EDS analysis performed for areas marked by square symbols in Fig. 1.

Place of analysis	Element [at. %]					
	Al	Nb	Hf	Sc	Ti	Zr
1	15.1 ± 1.9	5.1 ± 2.2	23.6 ± 1.4	9.1 ± 3.1	24.4 ± 0.6	22.7 ± 2.1
2	20.5 ± 1.4	4.6 ± 1.3	19.2 ± 0.3	10.2 ± 1.9	23.4 ± 2.3	22.1 ± 2.9
3	15.0 ± 2.0	5.4 ± 2.2	18.6 ± 0.9	13.4 ± 1.5	23.4 ± 2.1	24.2 ± 2.0

in β-Ti alloys, where there is a strong stabilizer in the bcc structure [25]. A similar effect is observed in the present multicomponent alloys. For instance, Lilensten et al. [30] have shown that an alloy of a similar composition (i.e. $Ti_{35}Zr_{27.5}Hf_{27.5}Nb_5Ta_5$) had a stable single bcc structure. The results prove that Ta and Nb enhance the formation of the body-centered cubic structure [28,30].

For precise characterization of the $Al_{10}Hf_{25}Nb_5Sc_{10}Ti_{25}Zr_{25}$ at.% HEA microstructure, the TEM analysis in the BF mode has been carried out. Fig. 3 shows the resulting TEM bright field image, which allows the identification of a very fine needle-like structure with the thickness up to 50 nm and length of about 1 μm. The preferential directions of the growth of plates in the matrix are clearly visible at the intersection angle of 57°. The results of the examinations performed with the selected area electron diffraction patterns (SAEDP), which are shown in Fig. 4a–c, indicate that the microstructures of the matrix and needles are of the bcc- and orthorhombic-type, respectively. Their morphologies are typical for the martensitic structures, which are presumably formed during the diffusionless transformation induced by rapid cooling (about 100 °C/s) just after arc melting. The martensite phase of titanium alloys may split into the hexagonal α' martensite or orthorhombic α'' structure [25]. In the as-cast TiZrHf alloy, where the bcc-to-hcp (β→α) polymorphic transformation takes place, only the α phase laths having different crystal orientations and being few micrometers in size are usually identified. The differences in relation to the results presented in the work are associated with the lack of elements stabilizing the β-phase. For example, the $Ti_{40}Zr_{20}Hf_{10}Nb_{20}Ta_{10}$ at.% HEA after casting contains a single bcc phase due to high content of Nb and Ta [53].

To obtain an insight of the microstructure of the investigated HEA at the atomic level, the high-resolution transmission electron microscopy (HRTEM) imaging technique has been applied. The resulting HRTEM image of the plate area marked in Fig. 4a is shown in Fig. 5a. Fig. 5b and c presents the Fast Fourier Transform (FFT) of the HRTEM micrograph and the lattice reconstruction following from the inverse FFT, respectively. From the lattice distances and their mutual angles measured using FFT (Fig. 5c), the hcp [−111] zone-axis orientation was identified,
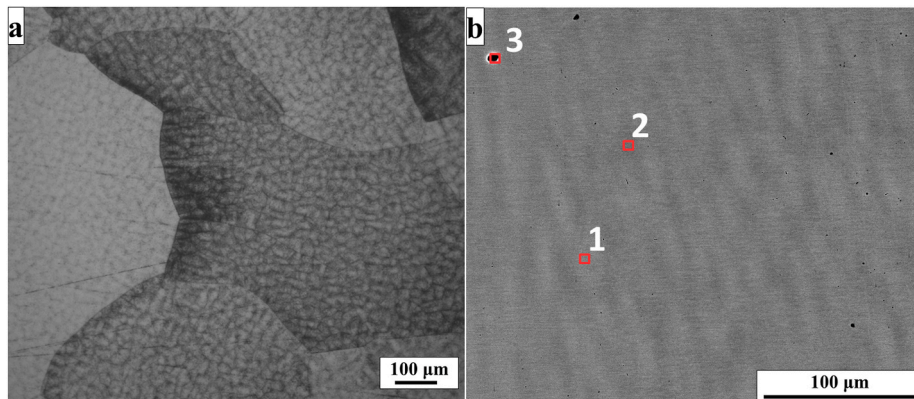

Fig. 1. (a) Light microscopy and (b) SEM images of the $Al_{10}Hf_{25}Nb_5Sc_{10}Ti_{25}Zr_{25}$ at.% HEA microstructure. Areas of the EDS analysis are marked by squares and presented in Table 1.
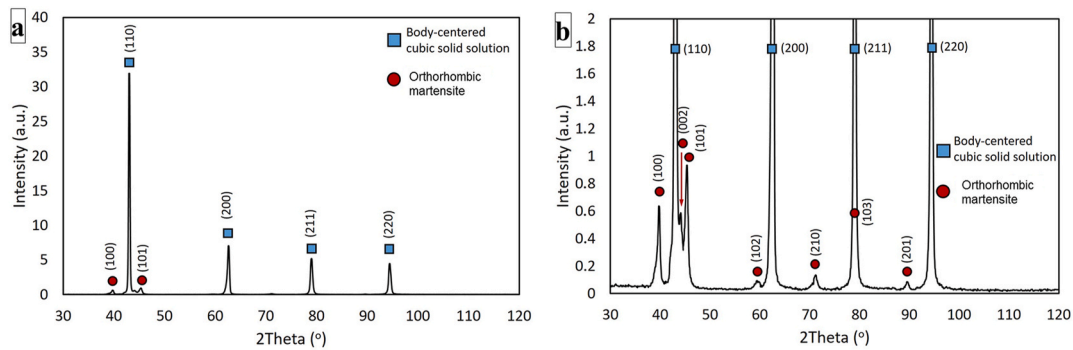
Fig. 2. **(a)** X-ray diffraction spectrum of the $Al_{10}Hf_{25}Nb_5Sc_{10}Ti_{25}Zr_{25}$ at.% HEA, **(b)** Enlarged spectral area showing low intensity spectral peaks corresponding to orthorhombic structure.

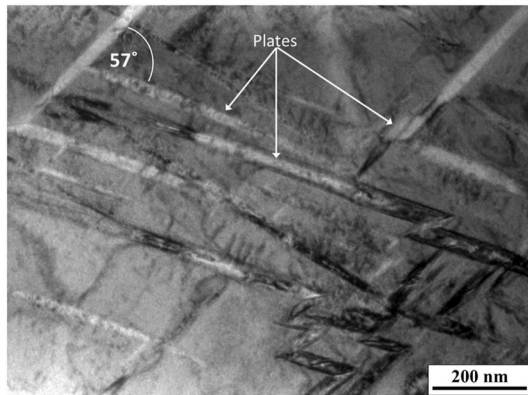**Fig. 3.** TEM-BF image of as-cast $Al_{10}Hf_{25}Nb_5Sc_{10}Ti_{25}Zr_{25}$ at.% alloy showing needle-like orthorhombic phase formed in the matrix of bcc structure.

which fitted well to the simulation of the reciprocal lattice section at that orientation. The packets of subplates with high angle boundaries are visible in the HRTEM image (Fig. 5a). The inverse FFT (Fig. 5c) obtained with the use of the Digital Micrograph software, by applying "masks" near the reflections in the FFT, showed much better contrast. High density of defects, observed as changes in the contrast, e.g. edge or complex dislocations are well visible in the Fourier filtered part of the image. In addition, the usage of masks for the chosen spots in the inverse FFT allowed obtaining a Fourier filtered image in certain

crystallographic directions. Additionally, an area with strong defects and numerous edge dislocations between the subplates can be noticed. Such defects could be as well responsible for the effect of hardening.

In order to determine the distribution of elements in the area of needles, a qualitative chemical analysis was performed using a STEM mode (see Fig. 6). Little bright contrast features can be distinguished within the darker matrix in Fig. 6a, which represents the area of small plates. The analyzed area is marked by frame and the results are shown in the form of maps of distributions of individual elements that are depicted in Fig. 6b–g. The observed homogeneous distribution of all elements suggests diffusionless character of the needle formation. Moreover, the line scan of chemical composition has been carried out in the direction perpendicular to the longitude axis of needles (Fig. 7). The STEM image shows changes in the contrast related to the plates having different crystallographic relation with respect to the matrix, but no significant changes in composition can be observed. This also confirms the diffusionless mode of the transformation leading to the formation of plate-like morphology.

3.2. Effect of temperature on microstructure and properties

In order to determine the influence of temperature on microstructure and mechanical properties of the $Al_{10}Hf_{25}Nb_5Sc_{10}Ti_{25}Zr_{25}$ at.% HEA, annealing at 1000 °C for 5 h was conducted using the DSC analysis (Fig. 8). The heat flow curve showed an endothermic effect in the range of 830–920 °C, which was probably associated with the transformation from the bcc to hcp structure. Further heating resulted in the exothermic
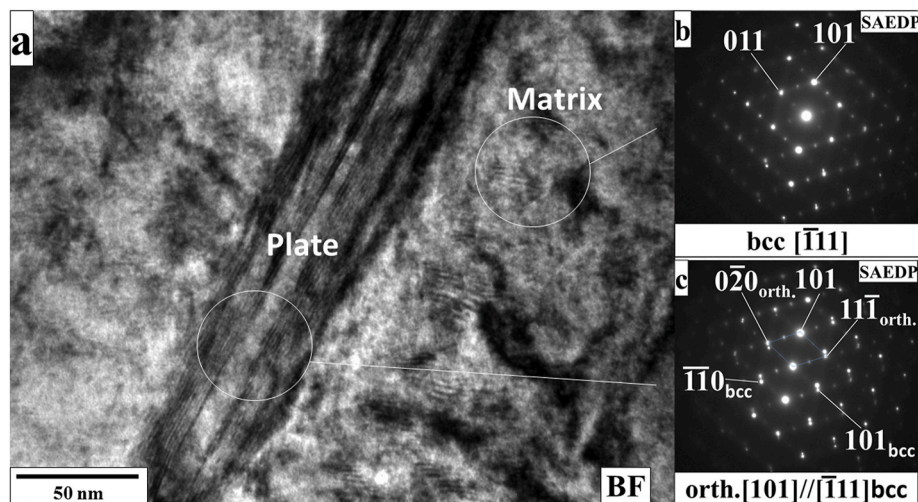

Fig. 4. **(a)** TEM bright field image of as-cast $Al_{10}Hf_{25}Nb_5Sc_{10}Ti_{25}Zr_{25}$ at.% HEA, **(b)** SAEDP from bcc structure matrix, **(c)** SAEDP from both matrix and orthorhombic structure of the needle. Crystallographic relation between bcc and orthorhombic lattices is shown in **(c)**.
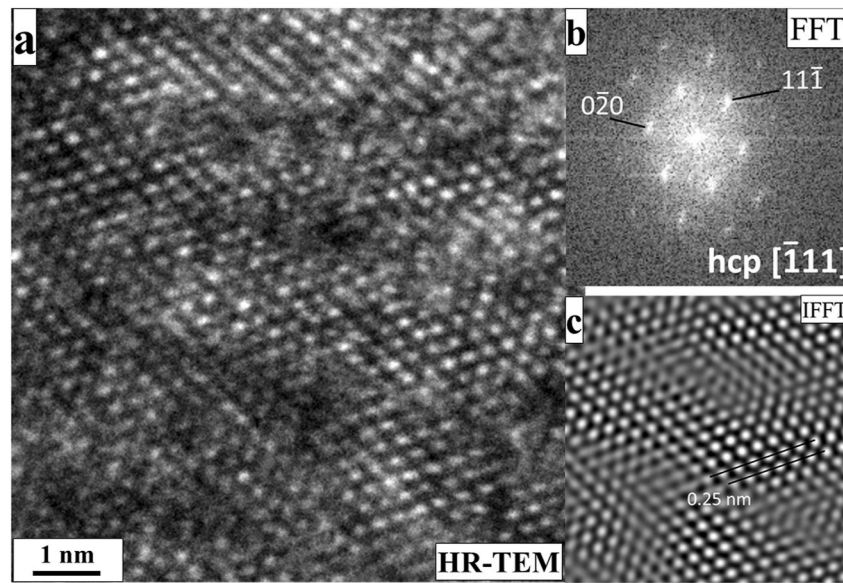
Fig. 5. (a) HRTEM image of area of needles in as-cast $Al_{10}Hf_{25}Nb_5Sc_{10}Ti_{25}Zr_{25}$ at.% alloy, **(b)** Fourier transform of HRTEM image, and **(c)** lattice reconstruction by inverse FFT (IFFT).
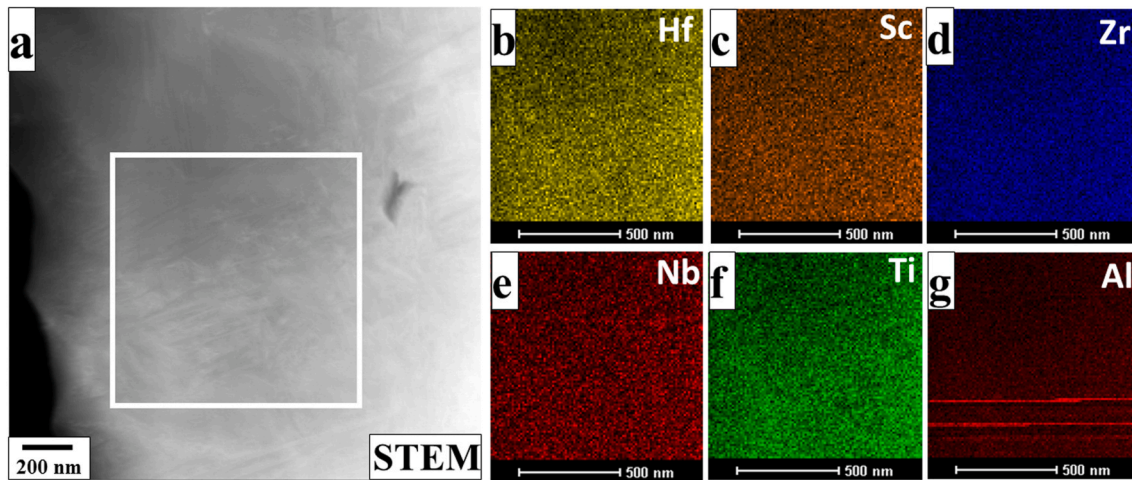

Fig. 6. (a) STEM image of $Al_{10}Hf_{25}Nb_5Sc_{10}Ti_{25}Zr_{25}$ at.% alloy as cast condition; (b)–(g) surface distributions of alloy constituents (Hf, Sc, Zr, Nb, Ti, Al).

reaction between 1270 and 1310 °C, which was probably caused by the formation of the $(Zr, Sc)_3Al$, $(Zr, Sc)Al_3$, $(Zr, Sc)_2Al$ like precipitates. In consequence, annealing at 1000 °C for 5h, *i.e.* in the temperature range above the first endothermic effect led to the homogenization of composition. Thus, the sample cooled in the furnace remained closer to the thermodynamic equilibrium than that directly cast. Additionally, slow cooling enhanced the diffusion transformation of titanium. The XRD analysis (Fig. 9) of the sample after annealing, which is displayed in Fig. 9, confirms the presence of about 30 vol% of the bcc phase (Im-3m space group, a ≈3.4472 Å), while the remaining amount corresponds to the hcp lattice ($P6_3/mmc$ space group, a ≈3.181 Å, c ≈ 5.004 Å). The BSE images of the material microstructure after annealing at 1000 °C for 5 h are shown in Fig. 10, whereas the results of the EDS analysis are collected in Table 2. The microstructure consists of large grains with average size up to 2 mm. The BSE picture shows a composition contrast of two phases. The "darker" phase (matrix) with the volume fraction of 32% reveals an increased content of Nb and Ti (see point 1 in Fig. 10 b and Table 2). The "brighter" phase with the plate-like morphology extending up to 150 µm of length and 10 µm thick, is enriched with Zr, Sc, and Hf, at the expense of Nb and Ti (see point 2 in Fig. 10 b and

Table 2). The "brighter" phase occupies mainly elongated narrow grains, which are either oriented parallel to each other or intersect at angles close to 60° (Fig. 10). Such morphology suggests that the grains of the "brighter" phase may share a common crystallographic relationship between each other. Moreover, the applied annealing leads to the formation of small precipitates with the average size of 1.5–3 µm that are enriched Sc (see point 3 in Fig. 10 b and Table 2). Relating the present results to those obtained for the annealed $Nb_{25}Sc_{25}Ti_{25}Zr_{25}$ alloy [9], which evidenced phase separation into β-NbZrTi and α(Sc, Zr), it may suggest that the addition of Nb should enhance the phase separation process in the $Al_{10}Hf_{25}Nb_5Sc_{10}Ti_{25}Zr_{25}$ at.% HEA due to a complete lack of the mutual solubility of scandium and niobium.

The EBSD orientation analysis is presented in Fig. 11. It reveals that the narrow, elongated grains of hexagonal phase are surrounded by the remaining cubic structure. The crystallites of the hexagonal phase are organized in the form of clusters, characterized by the same crystallographic and spatial orientations as the constituent needle-like grains. These results suggest that all grains belonging to the particular cluster originate from the same parent grain of the cubic structure. The conclusion is confirmed by the detailed inspection of the orientation
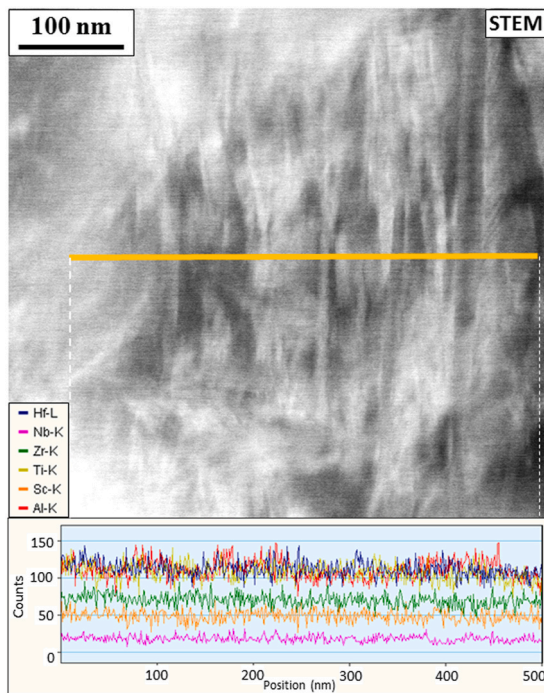
Fig. 7. Line scan analysis from area of plate-like structures in as-cast $Al_{10}Hf_{25}Nb_5Sc_{10}Ti_{25}Zr_{25}$ at.% HEA.
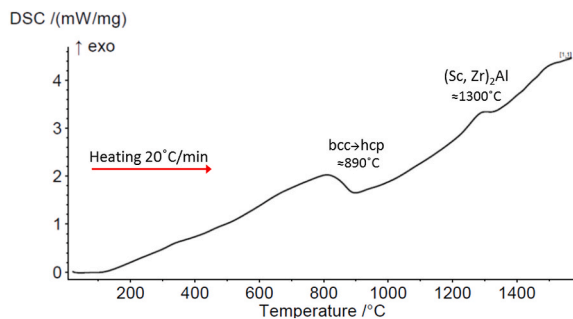
Fig. 8. DSC heat flow curve of as-cast $Al_{10}Hf_{25}Nb_5Sc_{10}Ti_{25}Zr_{25}$ at.% HEA.
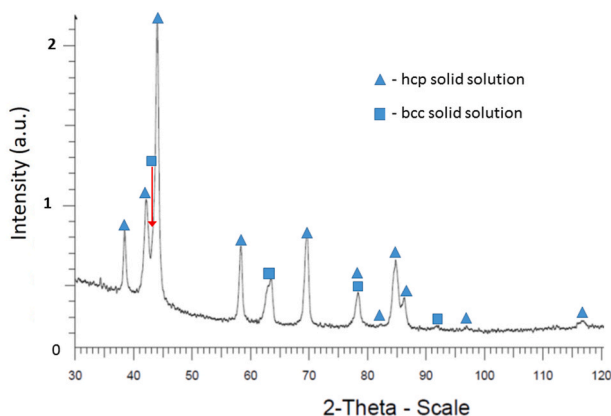
Fig. 9. X-ray diffraction patterns of $Al_{10}Hf_{25}Nb_5Sc_{10}Ti_{25}Zr_{25}$ at.% HEA after annealing at 1000 °C for 5 h.

map containing solely cubic structure (Fig. 11b). It revealed that primary grains of the phase could have been of few hundreds of microns in diameter.

A detailed analysis of misorientations between cubic and hexagonal crystallites showed that there was a very common misorientation of nearly 45° about axis <20–11 9 3> of hexagonal or <25 3 2> of cubic systems. In order to approximately visualize this phenomenon, grain boundaries with 45° ± 2° misorientation (however, with no respect to the rotation axis) were plotted with black line in Fig. 11a. As it can be seen, the black contour outlines most of the grains what indicates that this kind of boundary is very common in the investigated material.

Such observations suggest that upon annealing at 1000 °C, diffusion of the constituent elements in the $Al_{10}Hf_{25}Nb_5Sc_{10}Ti_{25}Zr_{25}$ at.% alloy led to their segregation, which later resulted in the phase transformation from the cubic to hexagonal structure. Such transformation could take place either during the annealing process, as a simple result of altering chemical composition, or while the sample was cooled down to ambient temperature. The obtained hexagonal phase retained the crystallographic relationship with the parental cubic structure.

The TEM observations, presented in Fig. 12, allowed the detailed determination of the phase composition of the alloy after annealing. The BF image shows a complex contrast created by the crystallographic orientations and chemical composition, and suggests the presence of two phases. The plate-like morphology up to 1 μm thick of the solid solution can be seen within the matrix. The SAEDP from the region marked by the ring in Fig. 12 a shows (002) and (020) spots of the body cubic centered solid solution, corresponding to the [100] zone axis (Fig. 12 b). The SAEDP from the area of plates, marked by ring in Fig. 12 a, confirmed the existence of the hexagonal solid solution with the [210] zone axis.

It should be noted that, in some cases, the hcp structure presented in Fig. 10a and b has a morphology that looks like split strands needles within the bcc matrix, which forms bands like the structures of both the bcc and hcp phases (description concerns internal single bands of the hcp phase). The bcc band within the hcp laths is also visible in the STEM image depicted in Fig. 13. The second plate, to be seen along the area of the interface as giving a brighter contrast, is the result of different composition. Its characteristic morphology is typical for twins in (α') martensite [25]. The line scan analysis of the chemical composition has been carried out along the area of the bcc and the hcp phases (see bottom part of Fig. 13). The diffusional character of phase separation should be noted. This result is, however, entirely distinct from that obtained for the as-cast state. The newly formed plates in the area of the bcc and hcp boundary nucleated probably in a heterogeneous manner due to local changes in the chemical composition and increased local strain.

Next, STEM investigations of the $Al_{10}Hf_{25}Nb_5Sc_{10}Ti_{25}Zr_{25}$ at.% alloy after annealing were conducted (Fig. 14). The area of the internal part of hcp plates (Fig. 10b), where there are visible split strands needles, was analyzed. The analysis showed that the bcc phase gave a lighter contrast, indicating that it was built of heavier atoms than the darker hcp phase. The accompanying qualitative EDS measurements confirmed that the highest Nb and Ti concentration was in the area of the darker bands, while the Hf, Sc, Zr and Al were located in between them. The above results were consistent with the X-ray analysis confirming the presence of two separate solid solutions: bcc and hcp. Small differences in the chemical compositions are visible when the results are compared with the SEM point analysis (increased concentration of Ti in the bcc phase as well as no changes in the Al content). The differences between the applied methods are the result of the analysis accuracy connected with the penetration depth of the beam. Nevertheless, divorce Nb between the phases exerts the highest impact on the type of the formed structure.

3.3. Mechanical properties

Room temperature tensile strength testing was carried out to determine the deformation mode of the $Al_{10}Hf_{25}Nb_5Sc_{10}Ti_{25}Zr_{25}$ at.% alloy. The stress–strain plots for the as-cast state (continuous line) and after annealing at 1000 °C for 5 h (dashed curve) are shown in Fig. 15a. An evident difference in the behavior of the as-cast and annealed $Al_{10}Hf_{25}Nb_5Sc_{10}Ti_{25}Zr_{25}$ at.% alloy is observed. For the as-cast state, an
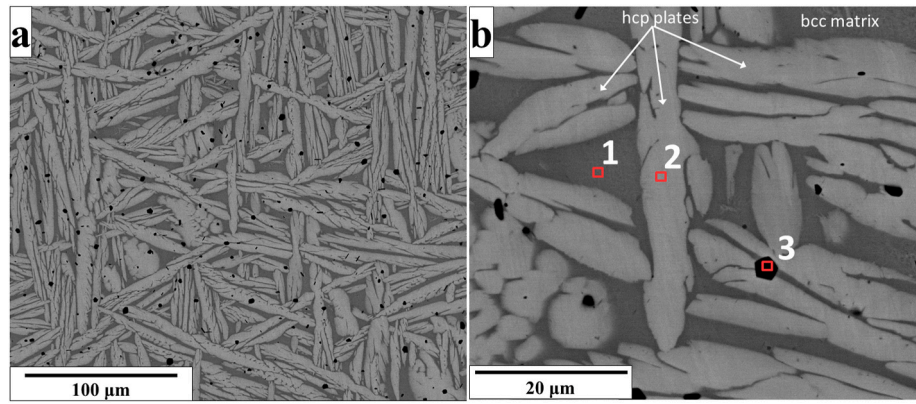
Fig. 10. SEM/BSE images of the $Al_{10}Hf_{25}Nb_5Sc_{10}Ti_{25}Zr_{25}$ at.% HEA after annealing for 5 h at 1000 °C **(a)** low magnification and **(b)** large magnification. Regions of the EDS analysis are marked with squares.

Table 2
Results of the EDS analysis for points 1-3 marked in Fig. 10 b.

Point of analysis	Element [at. %]					
	Al	Zr	Nb	Sc	Ti	Hf
1	14.6 ± 2.9	21.9 ± 0.4	10.2 ± 0.4	4.7 ± 0.9	29.3 ± 1.2	19.3 ± 0.4
2	14.4 ± 2.9	26.3 ± 0.5	3.2 ± 0.6	9.9 ± 2.0	18.9 ± 0.8	27.3 ± 0.5
3	5.5 ± 1.1	7.6 ± 0.3	3.0 ± 0.6	62.7 ± 1.3	12.0 ± 0.5	9.2 ± 0.2

average tensile strength reaching 900 MPa, (continuous curve) is accompanied by the strain of 4.2%, while the yield strength and hardness amount to 500 MPa and 390 HV, respectively. Annealing leads to significant increase of the tensile strength, reaching up to 1240 MPa, while the yield strength and plasticity increase to 660 MPa and 11.5%, respectively. The hardness of the sample increases to 485 HV. The different mechanical responses between as cast and annealed state can be attributed to different crystal structures of the studied alloys.

The as-cast $Al_{10}Hf_{25}Nb_5Sc_{10}Ti_{25}Zr_{25}$ sample during the uniaxial compression tests (Fig. 15b) showed a dual-yielding effect with the "primary" yield point of 620 MPa, fracture strength of 2132 MPa, and the overall plastic strain of 20%. The results suggest a bcc-to-α' phase transformation during compression as well as twins formation. It seems that there is a potential to develop a transformation induced plasticity effect in these alloys (TRIP). After the annealing of the sample, it revealed 1940 MPa at the yield strength of 1168 MPa. Significant differences between the compression and tensile behavior are connected with the anisotropy of mechanical properties, which is commonly observed in other alloys.

The hardness of the as-cast and subsequently annealed alloy increase to 520 HV and 540 HV for the samples elongated by ε = 4.2% and 11.5%, respectively. Significant increase of hardness for the annealed and strained sample is related to the formation of deformation twins, which strengthen the alloy. Similar effect was observed in Zr forged bar, which revealed strong hardening effect after deformation due to the presence of twins, which acted as effective barriers to the dislocation motion or created the regions of preferential slip [54]. For comparison, the pure Ti with alpha phase of hexagonal structure exhibits yield strength (YS) from 250 to 400 MPa and high plasticity reaching 40% due to twinning and slip. Such mechanism was proved to be an important deformation mode at room temperature [55–57]. In the present study it should be assumed that the higher YS and strength obtained by the deformation are due to large solid solution hardening within the heavily distorted lattice.

In the next stage of studies, the microstructural observations have been carried out near the fracture area of the tensile strength samples. Figs. 16–18 display results of these investigations. For the as-cast state, the TEM-BF studies (Fig. 16a) show deformation bands with the thickness ranging from 50 to 300 nm and length of several hundred nanometers (tensile strength sample). The selected area diffraction patterns
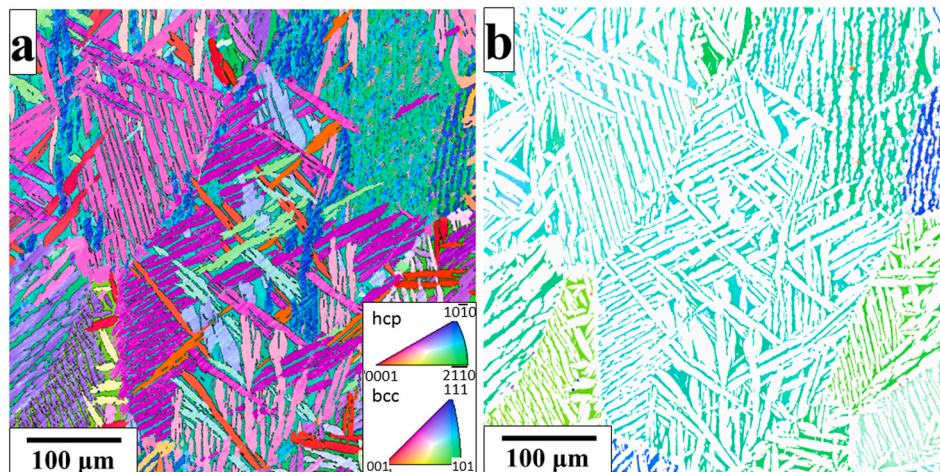

Fig. 11. EBSD orientation maps of $Al_{10}Hf_{25}Nb_5Sc_{10}Ti_{25}Zr_{25}$ at.% HEA after annealing at 1000 °C during 5 h (a) Orientation map of both identified phases. Black outline denotes 45° boundaries. (b) Orientation map of the cubic phase only. Inverse pole figure (IPF) coloring scheme is applied.
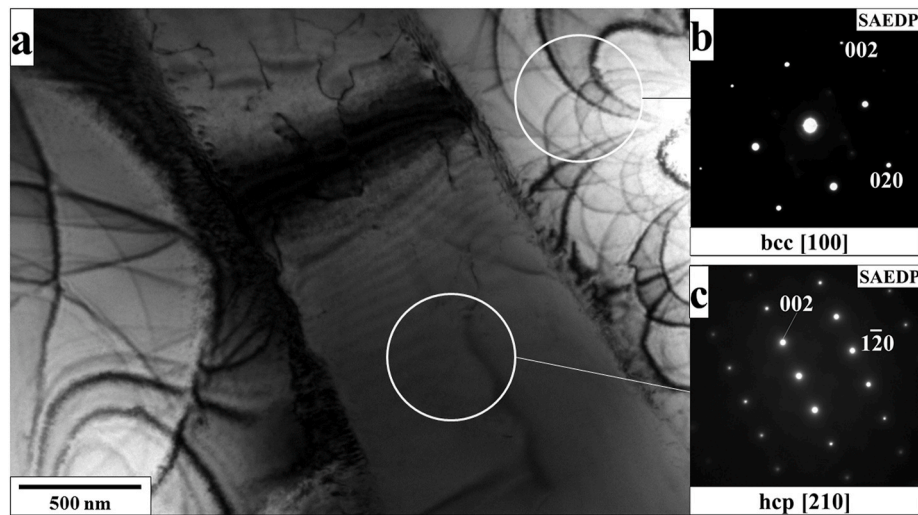
Fig. 12. (a) Bright field TEM image of $Al_{10}Hf_{25}Nb_5Sc_{10}Ti_{25}Zr_{25}$ at.% HEA annealed at 1000 °C for 5 h. SAEDP from (b) matrix and (c) plates.

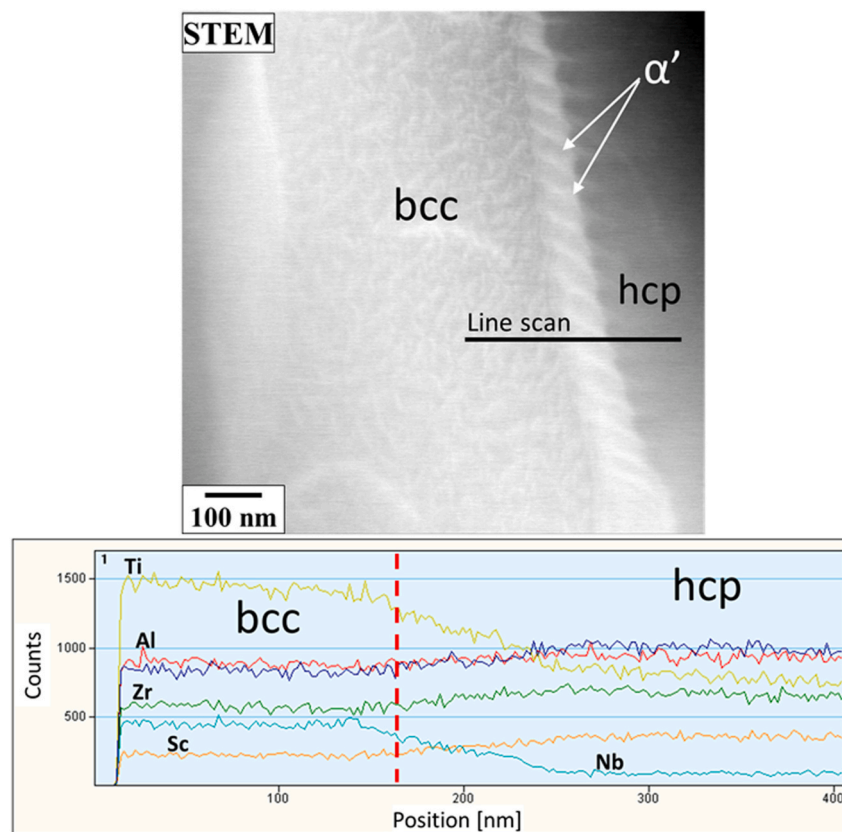**Fig. 13.** Line scan analysis from area of the plate-like morphology in $Al_{10}Hf_{25}Nb_5Sc_{10}Ti_{25}Zr_{25}$ at.% HEA after annealing.

from both adjacent bands show the bcc structures with the same orientation [111], which differ by a few degrees (Fig. 16b and c).

The fracture analysis of the annealed and strained (up to 11.5%) tensile strength sample, indicates that cracking can propagate between the clusters of hexagonal phase platelets. The arrow in Figs. 17 and 18a points at the crack that runs straight along the border between two regions, characterized by different spatial orientations of the hexagonal phase lamellae, which retain the same crystallographic orientation. Moreover, the twin-like morphology of the structure within the plates is identified (Fig. 18b). The TEM-BF image and SAEDP also confirm the presence of twins within the hcp plates (Fig. 19). Deformation twinning

of the hcp structure plays a crucial role in plastic deformation and strengthening of the materials [54,58]. To explain the above observation, let us assume that the platelets of the hexagonal phase may act as reinforcement in a composite material. In such a case, gaps and irregularities in spatial distribution of the reinforcement may create a path for crack propagation through the material. In the present study, the boundaries between two regions of different alignment of the hexagonal phase platelets might also play the role of a gap in the reinforcements, which facilitates fracture development. The {1011} twins have been observed only at relatively high deformation temperatures, i.e. above 400 °C for HCP titanium and zirconium alloys [59]. Similar twinning
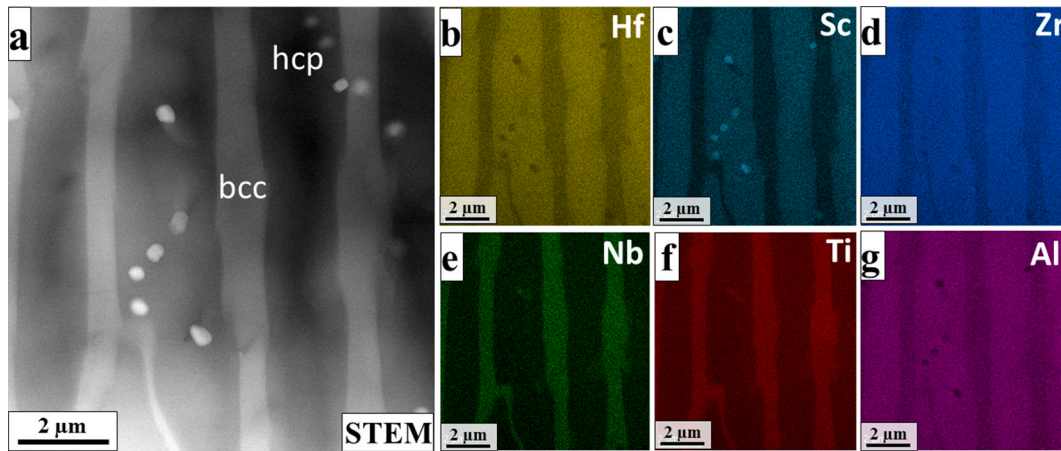
Fig. 14. (a) STEM image of $Al_{10}Hf_{25}Nb_5Sc_{10}Ti_{25}Zr_{25}$ at.% alloy after annealing; (b)–(g) surface distributions of the alloy constituents (Hf, Sc, Zr, Nb, Ti, Al).

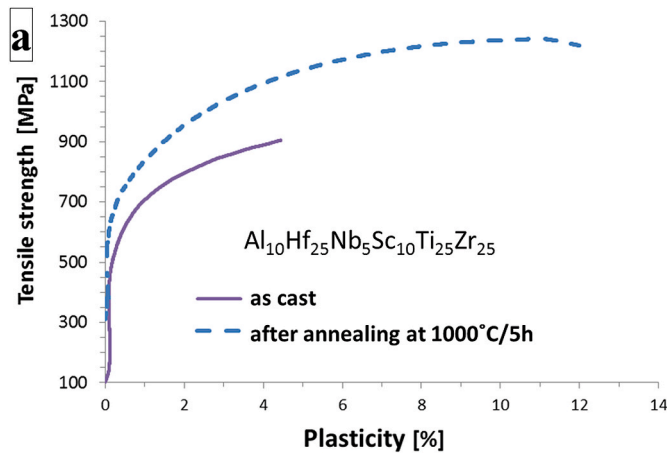**Fig. 15a.** Tensile strength curves for $Al_{10}Hf_{25}Nb_5Sc_{10}Ti_{25}Zr_{25}$ at.% alloy in as-cast state (continuous line) and after annealing at 1000 °C for 5h (dashed line).
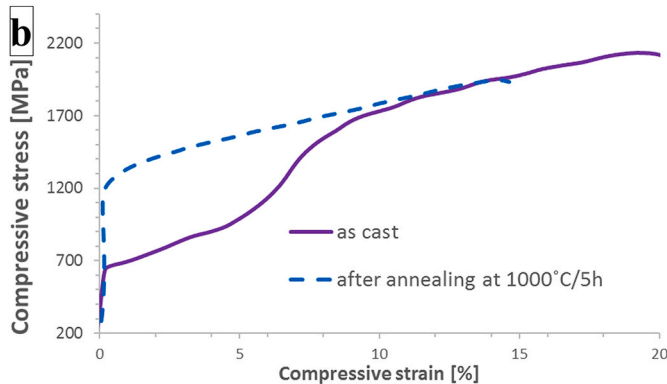

Fig. 15b. Compression curves of the $Al_{10}Hf_{25}Nb_5Sc_{10}Ti_{25}Zr_{25}$ at.% HEA as-cast (continuous line), and after annealing at 1000 °C for 5h (dashed line).

microstructure also appears along with the bcc→hcp martensitic transformation [60]. These transformation twins are also found in water quenched Ti–50Zr (at.%) alloy [61]. Another interesting aspect is related to the relatively high ductility of Al $_{10}Hf_{25}Nb_5Sc_{10}Ti_{25}Zr_{25}$ alloy. Generally, most of the Al-containing HEAs such as: AlxHfNbTaTiZr [62, 63], AlxNbTaTiV [64] or AlxCrNbTiVZr [65] are of low ductility or even brittle at room temperature. The brittleness is caused by ordered intermetallic phases, such as B2, Laves and Al–Zr phases, whose formation is

facilitated via the chemical interactions of aluminum with other alloying elements [13]. For example, many of these alloys have the ordered B2 matrix, while the disordered bcc phase is discontinuous [23–26]. The recent work of Senkov et al. [12] showed that the plasticity of $Al_{10}Nb_{15}Ta_5Ti_{30}Zr_{40}$ can be considerably improved by heat treatment, which breaks continuity of the B2 phase and results in the formation of disordered bcc matrix.

3.4. Analysis of alloy composition using d-electron approach

Lastly, the phase composition and mechanical behavior of the $Al_{10}Hf_{25}Nb_5Sc_{10}Ti_{25}Zr_{25}$ at.% alloy in the as-cast and annealed states can be analyzed by using the 'd-electron alloy design' method. Introduced by Morinaga et al. [66], this approach takes into account the bond order (Bo) and the metal d-orbital energy level (Md) parameters. It is traditionally applied to evaluate the stability of the bcc (β) phase in Ti alloys for the operation of different deformation modes, like dislocation slip, MBIP (MicroBand Induced Plasticity), TWIP (TWinning Induced Plasticity), or TRIP (TRansformation Induced Plasticity). Apart from the prognostication of deformation features of β alloys, the Bo-Md diagram also delineates the regions with the α and α+β structures. Several recent studies showed reasonable applicability of the Bo-Md diagram for Ti-containing HEAs demonstrating TRIP or MBIP effects [67–70]. Therefore, we reconstructed the Bo-Md diagram, collected numerous Ti-containing HEAs with either TRIP or MBIP effect, and several Ti alloys (Fig. 20). The $Al_{10}Hf_{25}Nb_5Sc_{10}Ti_{25}Zr_{25}$ at.% alloy with Bo ≈ 2.87 and Md ≈ 2.49 values locates under the M_s = RT line, to the right from the M_f = RT line. If the line separated the α and α+β fields could be extended following the same trend (dashed green line in Fig. 20), the $Al_{10}Hf_{25}Nb_5Sc_{10}Ti_{25}Zr_{25}$ at.% alloy would refer rather to the α field than to the α+β one. However, the lack of experimental data makes such extrapolation somewhat speculative. The α+β field with the TRIP effect seems more appropriate for the description of both appearances of diffusionless orthorhombic (α'' phase in terms of the Bo-Md map) and annealing induced hcp (α) phases in the bcc (β) phase. Moreover, the relocation of the $Al_{10}Hf_{25}Nb_5Sc_{10}Ti_{25}Zr_{25}$at.% alloy to the TRIP region correlates perfectly with the occurrence of somewhat transformation during plastic deformation indicated by the double-yielding phenomenon in the compression curve of the as-cast state (Fig. 15b). Thus, it can be suggested that the Bo-Md diagram is an adequate tool for predicting the structure and deformation mode of the $Al_{10}Hf_{25}Nb_5Sc_{10}Ti_{25}Zr_{25}$ at.% alloy. Meanwhile, further studies are highly needed to verify the applicability of the 'd-electron alloy design' method for search of new hcp/bcc HEAs, including the Al-Hf-Nb-Sc-Ti-Zr system, with advanced mechanical performance.
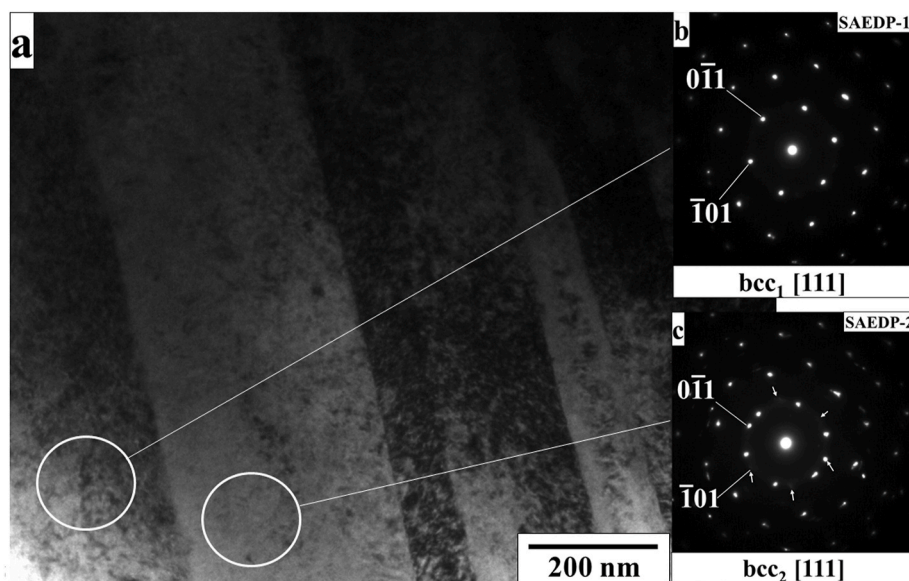
Fig. 16. (a) TEM bright field image of $Al_{10}Hf_{25}Nb_5Sc_{10}Ti_{25}Zr_{25}$ at.% as-cast alloy and corresponding SAED patterns after pre-straining to 4.2% from (b) marked area within shear band, and (c) marked area of adjacent bands.
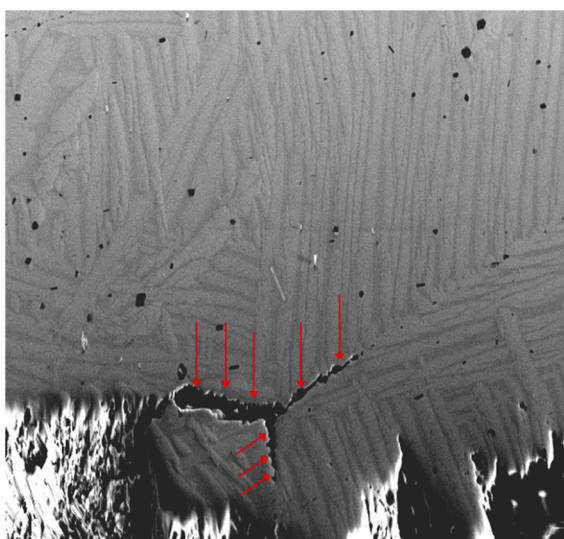

Fig. 17. SEM image of the fracture area. Red arrow indicates crack propagation along grain boundary of the sample after annealing. (For interpretation of the references to color in this figure legend, the reader is referred to the Web version of this article.)

3.5. Density functional theory studies

The results of the DFT calculations, including optimized lattice parameters, c/a, and b/a ratios of the bcc A2, hcp A3 and D0$_{19}$ as well as orthorhombic A$_{20}$ phases of $Al_{15}Hf_{25}Sc_{10}Ti_{25}Zr_{25}$ at.% and $Al_{10}Hf_{25}Nb_5Sc_{10}Ti_{25}Zr_{25}$ at.% HEAs are shown in Table 3. In general, the calculated structural parameters of the considered phases remain in reasonable agreement (about 2% or less) with those determined in the present X-ray diffraction experiments and the previous experimental studies [24]. The incorporation of 5 at.% of Nb atoms into the $Al_{15}Hf_{25}Sc_{10}Ti_{25}Zr_{25}$ at.% HEA has rather a minor effect on its lattice parameters. The calculated difference between motionless lattice energies ΔE_0 of the considered phases clearly indicates that the hcp A3 structure of the 5-component $Al_{15}Hf_{25}Sc_{10}Ti_{25}Zr_{25}$ at.% HEA is the most energetically stable at T = 0 K. The addition of 5 at.% of Nb atoms

stabilizes, however, the hcp D0$_{19}$ phase, whose energy becomes lower by 5 meV/atom than that of the hcp A3 phase. The difference in energies between the bcc A2 phase and the more stable hcp phase decreases upon enrichment the Al-Hf-Sc-Ti-Zr alloy with Nb. The zero-point energy motion F_{vib}(V, T = 0 K) arising from the lattice vibration is about 40 meV/atom for the hcp phases and the bcc A2 phase of $Al_{15}Hf_{25}Sc_{10}$-$Ti_{25}Zr_{25}$ at.% HEA, while it ranges between 25 and 28 meV/atom for the orthorhombic A$_{20}$ phases and the bcc A2 phase of $Al_{10}Hf_{25}Nb_5Sc_{10}$-$Ti_{25}Zr_{25}$ at.% HEA. At T = 0 K, the E_0 and F_{vib} contributions to the Helmholtz free energies of both alloys dominate, whereas the contribution from F_{el} remains negligible. The terms F_{el} and TS_{conf} become significant at elevated temperatures, and along with increasing contribution from the F_{vib} term at higher temperatures, govern temperature evolution of the energetic stability of HEAs' phases. Table 4 demonstrates schematically the energetic stability of particular phases in the selected temperature ranges. Our calculations show that the hcp structures are energetically favored over the bcc A2 or orthorhombic A$_{20}$ structures below 790K for $Al_{15}Hf_{25}Sc_{10}Ti_{25}Zr_{25}$ at.% HEA and 1150 K for $Al_{10}Hf_{25}Nb_5Sc_{10}Ti_{25}Zr_{25}$ at.% HEA. Above these temperatures the bcc A2 phases of both 5- and 6-component HEAs become energetically preferred. On the other hand, the orthorhombic A$_{20}$ structure remains least energetically stable up to 1350 K in $Al_{15}Hf_{25}Sc_{10}Ti_{25}Zr_{25}$ at.% HEA and 2000 K in $Al_{10}Hf_{25}Nb_5Sc_{10}Ti_{25}Zr_{25}$ at.% HEA.

The considered cubic, hexagonal and orthorhombic phases satisfy the Born stability criteria, which indicates their mechanical stability. The calculated polycrystalline elastic moduli (bulk modulus B, shear modulus G, Young' modulus E) along with the Poisson's ratio ν, Pugh's ratio k, and Vickers hardness H_V for the bcc, hcp, and orthorhombic phases of $Al_{15}Hf_{25}Sc_{10}Ti_{25}Zr_{25}$ at.% and $Al_{10}Hf_{25}Nb_5Sc_{10}Ti_{25}Zr_{25}$ at.% HEAs are listed in Table 5. Additional column containing parameters averaged over both hexagonal structures is included in Table 5. It is used to facilitate convenient comparison of the calculated mechanical properties of the hexagonal, cubic, and orthorhombic phases among each other. Such averaging is justified by a small difference in the Helmholtz free energies between the hcp A3 and D0$_{19}$ phases. The averaged values of the E, ν, k, and H_v parameters are derived from the respective arithmetic means for the B and G parameters.

Among the considered phases of the 5- and 6-component HEAs, their orthorhombic A$_{20}$ phases are the least resistant to compression, shear forces, and longitudinal stresses, as indicated by their relatively low bulk, shear, and Young's moduli. Generally, these phases can be
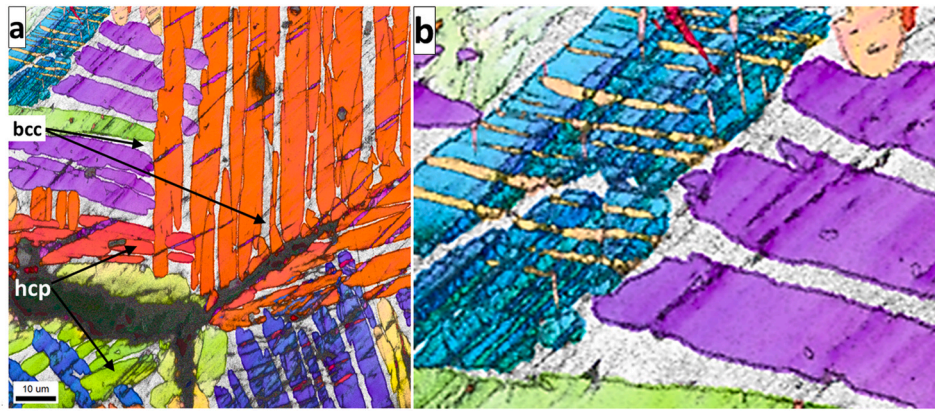
Fig. 18. (a) EBSD orientation maps of fracture surface for annealed sample. (b) Enlarged fragment of microstructure. IPF coloring scheme is applied.
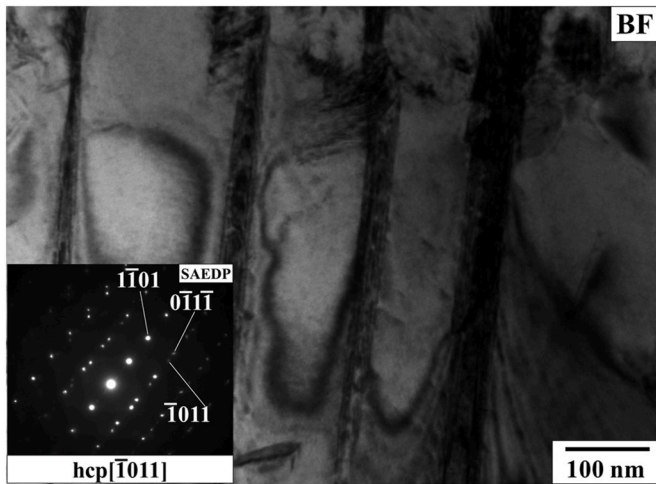

Fig. 19. TEM bright field image of $Al_{10}Hf_{25}Nb_5Sc_{10}Ti_{25}Zr_{25}$ at.% HEA from area of fracture surface of sample after annealing with inset of corresponding SAED pattern.

regarded as soft materials due to low values of their Vickers hardness. All these phases are expected to behave in a ductile manner, as suggested by their Pugh's ratios (k < 0.5) and Poisson's ratios ($\nu \sim$ 0.33) [71], which are common indicators of brittleness/ductility of a material. On the other hand, the bcc and hcp phases of both 5- and 6-component HEAs exhibit much higher values of their bulk, shear, and Young's moduli in comparison with the orthorhombic phases, which finally results in their much higher Vickers hardness. The bcc and hcp phases of $Al_{15}Hf_{25}Sc_{10}Ti_{25}Zr_{25}$ at.% and $Al_{10}Hf_{25}Nb_5Sc_{10}Ti_{25}Zr_{25}$ at.% HEAs are predicted to be more brittle than the orthorhombic phases, as evidenced by their Pugh's (Poisson's) ratios which are slightly higher (lower) than 0.5 (0.33). Upon addition of 5 at.% of Nb into the Al-Hf-Sc-Ti-Zr HEA, the bulk, shear and Young's moduli of the bcc phase increase by about 2–3%, whereas they become reduced by 1–5% for the hexagonal phase. Also, reduction of these parameters by several percent is observed for the Nb-doped orthorhombic phase. The phases do not undergo transition to a different brittle/ductile state when enriched in 5 at.% of Nb. The enrichment in Nb affects, however, the Vickers hardness of the hexagonal and orthorhombic phases, leaving H_v of the bcc phase almost unchanged. The H_v of hexagonal phase with 5 at.% of Nb is reduced by $\sim$10%. The most substantial decrease in H_v upon incorporated Nb is observed for the orthorhombic A_{20} phase, for which its Vickers hardness undergoes reduction by almost twice. We should, however, note that the
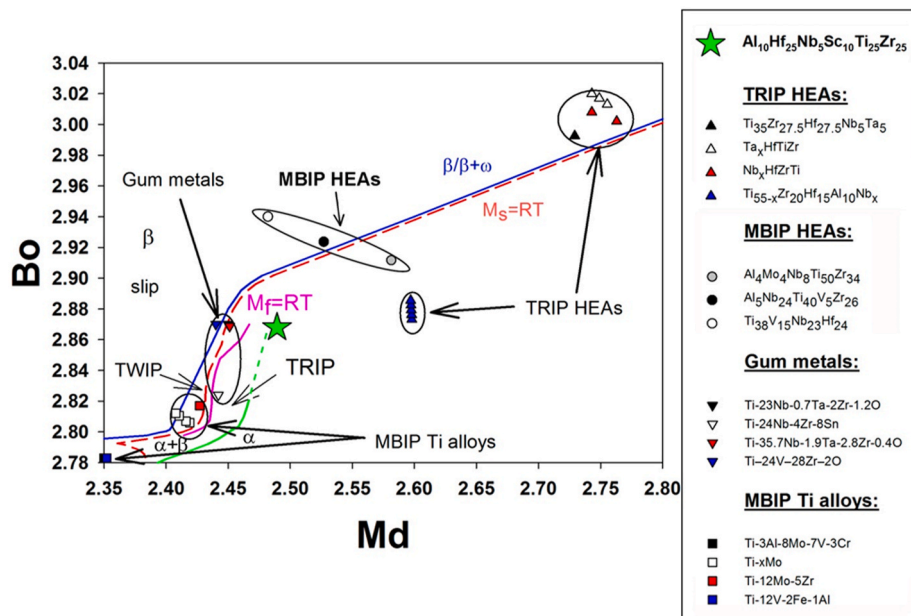

Fig. 20. Positions of the $Al_{10}Hf_{25}Nb_5Sc_{10}Ti_{25}Zr_{25}$ at.% alloy, several TRIP and MBIP Ti-containing HEAs, and some Ti alloys on the Bo-Md diagram.

Table 3

Calculated structural parameters and relative energies ΔE_0 and ΔF at T = 0 K of the bcc, hcp and orthorhombic phases of $Al_{15}Hf_{25}Sc_{10}Ti_{25}Zr_{25}$ at.% and $Al_{10}Hf_{25}Nb_5Sc_{10}Ti_{25}Zr_{25}$ at.% HEAs. Numbers in brackets denote experimental values determined in the present and previous X-ray diffraction measurements [24]. Relative energies (in meV/atom) are given with respect to the most stable phase, i.e., hcp A3 for $Al_{15}Hf_{25}Sc_{10}Ti_{25}Zr_2$ at.% HEA and hcp $D0_{19}$ for $Al_{10}Hf_{25}Nb_5Sc_{10}Ti_{25}Zr_{25}$ at.% HEA.

Quantity	bcc A2	hcp A3	hcp $D0_{19}$	orthorhombic A_{20}
$Al_{15}Hf_{25}Sc_{10}Ti_{25}Zr_{25}$ at.% HEA				
a (Å)	3.4608	3.0880	3.0875	2.9808
		(3.1092)	(3.1126)	
c/a	1	1.59 (1.585)	1.59 (1.593)	1.898
b/a	1	1.59	1.59	1.760
ΔE_0	+51	0	+14	+98
ΔF	+33	0	+9	+83
$Al_{10}Hf_{25}Nb_5Sc_{10}Ti_{25}Zr_{25}$ at.% HEA				
a (Å)	3.4610	3.0966	3.0948	2.9792 (3.034)
	(3.448)			
c/a	1	1.59	1.59	1.898 (1.898)
b/a	1	1.59	1.59	1.760 (1.760)
ΔE_0	+33	+5	0	+99
ΔF	+34	+6	0	+86

Table 4

Energetic stability of the bcc A2, hcp A3, hcp $D0_{19}$, and orthorhombic A_{20} phases of $Al_{15}Hf_{25}Sc_{10}Ti_{25}Zr_2$ at.% and $Al_{10}Hf_{25}Nb_5Sc_{10}Ti_{25}Zr_{25}$ at.% HEAs in selected temperature ranges. Phases are ordered according to their Helmholtz free energies F(V,T).

Temperature range (K)	Sequence of phases
$Al_{15}Hf_{25}Sc_{10}Ti_{25}Zr_{25}$ at.% HEA	
0–720	F (A3) < F ($D0_{19}$) < F (A2) < F (A_{20})
720–790	F (A3) < F (A2) < F ($D0_{19}$) < F (A_{20})
790–950	F (A2) < F (A3) < F ($D0_{19}$) < F (A_{20})
950–1350	F (A2) < F ($D0_{19}$) < F (A3) < F (A_{20})
1350–2000	F (A2) < F ($D0_{19}$) < F (A20) < F (A3)
$Al_{10}Hf_{25}Nb_5Sc_{10}Ti_{25}Zr_{25}$ at.% HEA	
0–1080	F ($D0_{19}$) < F (A3) < F (A2) < F (A_{20})
1080–1100	F (A3) < F ($D0_{19}$) < F (A2) < F (A_{20})
1100–1150	F (A3) < F (A2) < F ($D0_{19}$) < F (A_{20})
1150–2000	F (A2) < F (A3) < F ($D0_{19}$) < F (A_{20})

Table 5

Theoretical bulk modulus B, shear modulus G, Young's modulus E = 9BG/(3B + G), Poisson's ratio ν=(3B−2G)/(6B+2G), Pugh's ratio k = G/B, Vickers hardness $H_V = 2 (k^2 G)^{0.585}$-3 [50] for the bcc A2, hcp A3, hcp $D0_{19}$, and orthorhombic A_{20} phases of $Al_{15}Hf_{25}Sc_{10}Ti_{25}Zr_{25}$ at.% and $Al_{10}Hf_{25}Nb_5Sc_{10}Ti_{25}Zr_{25}$ at.% HEAs. The column denoted as hcp average contains values averaged over both hexagonal structures (see text for details).

Quantity	bcc A2	hcp A3	hcp $D0_{19}$	hcp average	orthorhombic A_{20}
$Al_{15}Hf_{25}Sc_{10}Ti_{25}Zr_{25}$ at.% HEA					
B (GPa)	145	155	137	146	98
G (GPa)	80	99	78	86	40
E (GPa)	203	245	197	216	106
ν	0.267	0.237	0.261	0.254	0.320
k	0.552	0.639	0.569	0.586	0.408
H_V (GPa)	9.954	14.415	10.225	11.581	3.063
$Al_{10}Hf_{25}Nb_5Sc_{10}Ti_{25}Zr_{25}$ at.% HEA					
B (GPa)	150	146	144	145	98
G (GPa)	82	83	80	82	34
E (GPa)	208	209	203	207	91
ν	0.269	0.261	0.267	0.262	0.345
k	0.547	0.568	0.556	0.566	0.347
H_V (GPa)	10.003	10.686	10.064	10.520	1.562

orthorhombic phase can hardly form due to its energetic instability in a wide temperature range.

4. Conclusions

The novel six-component $Al_{10}Hf_{25}Nb_5Sc_{10}Ti_{25}Zr_{25}$ at.% high entropy alloy having complex microstructure was developed and cast by arc melting from the elemental precursors. The present research demonstrates that.

1. The alloy in the as-cast state consists of large grains with size up to 1000 mm within bcc cell dendritic structure and dimensions of 20–40 μm. Very fine orthorhombic needle-like structure with thickness up to 50 nm and length reaching 1 μm is revealed within cell grains. They are formed by diffusionless transformation probably due to rapid cooling during crystallization. The orthorhombic-needles are arranged in preferential directions of intersection angle of 57° suggesting crystallographic dependence between them. The unique mixture of fine plates within bcc-matrix in the as-cast state leads to relatively high combination of strength and plasticity. The alloy with initial hardness of 390 HV reaches tensile strength of 900 MPa, yield strength of 500 MPa, and plasticity of 4.2%. Moreover sample during the uniaxial compression tests showed a dual-yielding effect with the "primary" yield point of 620 MPa, fracture strength of 2132 MPa, and the overall plastic strain of 20%. The results suggest a bcc-to-α' phase transformation during compression as well as twins formation.

2. The phase composition of $Al_{10}Hf_{25}Nb_5Sc_{10}Ti_{25}Zr_{25}$ alloy exhibits significant changes after annealing at 1000 °C for 5 h. The high-temperature gives rise to diffusional growth of hexagonal plates, which attain thickness of 10 μm and length up to 150 μm. In addition, plates reveal increased concentration of Zr, Sc and Hf at the expense of Nb and Ti. They are located within bcc phase enriched in Nb and Ti. Heat treatment results in significant increase of tensile strength up to 1240 MPa. Hardness amounts to 485 HV, whereas yield strength and plasticity are equal to 660 MPa and 11.5%, respectively.

3. The results and analysis of our *ab initio* calculations show that hexagonal phases of both $Al_{15}Hf_{25}Sc_{10}Ti_{25}Zr_{25}$ at% and $Al_{10}Hf_{25}Nb_5Sc_{10}Ti_{25}Zr_{25}$ at% HEAs are energetically favored over the bcc and orthorhombic phases at T = 0 K. These are brittle materials with relatively high Vickers hardness. The only ductile phase of the Al-Hf-Sc-Ti-Zr HEA is that having the orthorhombic A_{20} structure. Its ductility is retained after doping with 5 at.% of Nb. No change from a ductile to brittle state is observed neither for the cubic nor hexagonal phases after their enrichment in Nb. The hexagonal and orthorhombic phases of the Al-Hf-Sc-Ti-Zr HEA which contain 5 at.% of Nb have lower values of their bulk, shear, and Young's moduli as well as reduced values of H_v as compared to the respective values of the hexagonal and orthorhombic phases of the Nb-free alloy. Opposite effect, i.e., small increase in the B, G, E, and H_v parameters is encountered for the bcc A2 phase of the Al-Hf-Sc-Ti-Zr HEA after its doping with 5 at.% of Nb. Our calculations show that above 790 K for $Al_{15}Hf_{25}Sc_{10}Ti_{25}Zr_{25}$ at.% and 1150 K for $Al_{10}Hf_{25}Nb_5Sc_{10}Ti_{25}Zr_{25}$ at.% alloys their bcc A2 structures are more energetically stable than the A3 or $D0_{19}$ structures of hexagonal symmetries as well as A_{20} phases having orthorhombic structures.

CRediT authorship contribution statement

L. Rogal: Formal analysis, Conceptualization, Supervision, Writing - original draft, Visualization, prepared the manuscript, casting the alloys and performed the TEM studies, All authors approved the final manuscript for submission. **U.D. Wdowik:** Writing - review & editing, performed the ab initio simulations, All authors approved the final manuscript for submission. **M. Szczerba:** Formal analysis, Writing - review & editing, All authors approved the final manuscript for submission. **N. Yurchenko:** Formal analysis, All authors approved the final manuscript for submission. **T. Czeppe:** Formal analysis, All authors approved the final manuscript for submission. **P. Bobrowski:** performed

the SEM studies, All authors approved the final manuscript for submission.

Declaration of competing interest

The authors declare that they have no known competing financial interests or personal relationships that could have appeared to influence the work reported in this paper.

Acknowledgments

References

[1] J.W. Yeh, S.K. Chen, S.J. Lin, J.Y. Gan, T.S. Chin, et al., Nanostructured high-entropy alloys with multiple principal elements: novel alloy design concepts and outcomes, Adv. Eng. Mater. 6 (2004) 299–303, https://doi.org/10.1002/adem.200300567.

[2] B. Cantor, I.T.H. Chang, P. Knight, A.J.B. Vincent, Microstructural development in equiatomic multicomponent alloys, Mat. Sci. Eng. A-Struct. 375–377 (2004) 213–218, https://doi.org/10.1016/j.msea.2003.10.257.

[3] B.S. Murty, J.W. Yeh, S. Ranganathan, High-Entropy Alloys, first ed., Butterworth-Heinemann, Boston, 2014.

[4] Y. Zhang, T.T. Zuo, Z. Tang, M.C. Gao, K.A. Dahmen, et al., Microstructures and properties of high-entropy alloys, Prog. Mater. Sci. 61 (2014) 1–93, https://doi.org/10.1016/j.pmatsci.2013.10.001.

[5] H. Huang, Y. Wu, J. He, H. Wang, X. Liu, et al., Phase-Transformation ductilization of brittle high-entropy alloys via metastability engineering, Adv. Mater. 29 (2017), https://doi.org/10.1016/j.mtla.2020.100627, 1701-678.

[6] Y. Lu, Y. Dong, S. Guo, L. Jiang, H. Kang, et al., A promising new class of high-temperature alloys: eutectic high-entropy alloys, Sci. Rep. 4 (2014) 1–5, https://doi.org/10.1038/srep06200.

[7] L. Rogal, Y. Ikeda, M. Lai, F. Körmann, A. Kalinowska, et al., Design of a dual-phase hcp-bcc high entropy alloy strengthened by ω nanoprecipitates in the Sc-Ti-Zr-Hf-Re system, Mater. Des. 192 (2020) 108716, https://doi.org/10.1016/j.matdes.2020.108716.

[8] F. He, Z. Wang, P. Cheng, Q. Wang, J. Li, et al., Designing eutectic high entropy alloys of CoCrFeNiNbx, J. Alloys Compd. 656 (2016) 284–289, https://doi.org/10.1016/j.jallcom.2015.09.153.

[9] L. Rogal, J. Morgiel, Z. Swiatek, F. Czerwinski, Microstructure and mechanical properties of the new Nb25Sc25Ti25Zr25 eutectic high entropy alloy, Mater. Sci. Eng. 651 (2016) 590–597, https://doi.org/10.1016/j.msea.2015.10.071.

[10] L.J. Santodonato, Y. Zhang, M. Feygenson, C.M. Parish, M.C. Gao, et al., Deviation fromhigh-entropy configurations in the atomic distributions of a multi-principal-element alloy, Nat. Commun. 6 (2015) 5964, https://doi.org/10.1038/ncomms6964.

[11] M.C. Gao, J.W. Yeh, P.K. Liaw, Y. Zhang, High-Entropy Alloys: Fundamentals and Applications, Springer, Cham, 2016.

[12] O.N. Senkov, J.P. Couzinie, S.I. Rao, V. Soni, R. Banerjee, Temperature dependent deformation behavior and strengthening mechanisms in a low density refractory high entropy alloy Al10Nb15Ta5Ti30Zr40, Materialia 9 (2020), https://doi.org/10.1016/j.mtla.2020.100627, 100627.

[13] O.N. Senkov, D.B. Miracle, K.J. Chaput, J.P. Couzinie, Development and exploration of refractory high entropy alloys - a review, J. Mater. Res. 33/19 (2018) 3092–3128, https://doi.org/10.1557/jmr.2018.153.

[14] F. Maresca, W.A. Curtin, Mechanistic origin of high strength in refractory BCC high entropy alloys up to 1900K, Acta Mater. 182 (2020) 235–249, https://doi.org/10.1016/j.actamat.2019.10.015.

[15] D.B. Miracle, M.-H. Tsai, O.N. Senkov, V. Soni, R. Banerjee, Refractory high entropy superalloys (RSAs), Scripta Mater. 187 (2020) 445–452.

[16] V. Soni, O.N. Senkov, B. Gwalani, D.B. Miracle, R. Banerjee, Microstructural design for improving ductility of an initially brittle refractory high entropy alloy, Sci. Rep. 8 (2018) 8816, https://doi.org/10.1038/s41598-018-27144-3.

[17] T.M. Butler, K.J. Chaput, J.R. Dietrich, O.N. Senkov, High temperature oxidation behaviors of equimolar NbTiZrV and NbTiZrCr refractory complex concentrated alloys (RCCAs), J. Alloys Compd. 729 (2017) 1004–1019, https://doi.org/10.1016/j.jallcom.2017.09.164.

[18] T. Yang, Y.L. Zhao, Y. Tong, Z.B. Jiao, J. Wei, et al., Multicomponent intermetallic nanoparticles and superb mechanical behaviors of complex alloys, Science 362 (2018) 933–937, https://doi.org/10.1126/science.aas8815.

[19] O.N. Senkov, J.M. Scott, S.V. Senkova, D.B. Miracle, C.F. Woodward, Microstructure and room temperature properties of a high-entropy TaNbHfZrTi alloy, J. Alloys Compd. 509/20 (2011) 6043–6048, https://doi.org/10.1016/j.jallcom.2011.02.171.

[20] O.N. Senkov, A.L. Pilchak, S.L. Semiatin, Effect of cold deformation and annealing on the microstructure and tensile properties of a HfNbTaTiZr refractory high entropy alloy, Metall. Mater. Trans. 49A (2018) 2876, https://doi.org/10.1007/s11661-018-4646-8.

[21] H. Huang, Y. Wu, J. He, H. Wang, X. Liu, et al., Phase-transformation ductilization of brittle high-entropy alloys via metastability engineering, Adv. Mater. 9/30 (2017) 1–7, https://doi.org/10.1002/adma.201701678.

[22] S. Zherebtsov, N. Yurchenko, E. Panina, A. Tojibaev, M. Tikhonovsky, et al., Microband-induced plasticity in a Ti-rich high-entropy alloy, J. Alloys Compd. 842 (2020), https://doi.org/10.1016/j.jallcom.2020.155868, 155868.

[23] Ł. Rogal, F. Czerwinski, P.T. Jochym, L. Litynska-Dobrzynska, Microstructure and mechanical properties of the novel Hf25Sc25Ti25Zr25 equiatomic alloy with hexagonal solid solutions, Mater. Des. 92 (2016) 8–17, https://doi.org/10.1016/j.matdes.2015.11.104.

[24] L. Rogal, P. Bobrowski, F. Körmann, S. Divinski, F. Stein, et al., Computationally-driven engineering of sublattice ordering in a hexagonal AlHfScTiZr high entropy alloy, Sci. Rep. 7 (2017) 2209, https://doi.org/10.1038/s41598-017-02385-w.

[25] C. Leyens, M. Peters, Titanium and Titanium Alloys: Fundamentals and Applications, Wiley-VCH, Weinheim, 2003.

[26] M. Ashby, H. Shercliff, D. Cebon, K.J. Kurzydłowski, Inżynieria Materiałowa, Wydawnictwo Galaktyka, Cambridge, 2012.

[27] C.S. Liauo, H.C. Fu, I.C. Hsiao, J.C. Huang, On the β-transus and order/disorder transition temperature in superplastic super α2 Ti3Al base alloy, Mater. Sci. Eng. 271 (1999) 275, https://doi.org/10.1016/S0921-5093(99)00215-4.

[28] L. Wang, C. Fu, Y. Wu, R. Li, X. Hui, et al., Superelastic effect in Ti-rich high entropy alloys via stress-induced martensitic transformation, Scripta Mater. 162 (2019) 112–117, https://doi.org/10.1016/j.scriptamat.2018.10.035.

[29] V.S. Lyasotskaya, S.I. Knyazeva, Metastable phases in titanium alloys and conditions of their formation, Met. Sci. Heat Treat. 50/7–8 (2008) 373–377, https://doi.org/10.1007/s11041-008-9064-x.

[30] L. Lilensten, J.P. Couzinie, J. Bourgon, L. Perriere, G. Dirras, et al., Design and tensile properties of a bcc Ti-rich high-entropy alloy with transformation-induced plasticity, Mater. Res. Lett. 5/2 (2017) 110–116, https://doi.org/10.1080/21663831.2016.1221861.

[31] A. Zunger, S.-H. Wei, L.G. Ferreira, J.E. Bernard, Special quasirandom structures, Phys. Rev. Lett. 65 (1990) 353, https://doi.org/10.1103/PhysRevLett.65.353.

[32] G. Kresse, J. Hafner, Ab initio molecular dynamics for liquid metals, Phys. Rev. B 47 (1993) 558, https://doi.org/10.1103/PhysRevB.47.558.

[33] G. Kresse, J. Furthmüller, Efficiency of ab-initio total energy calculations for metals and semiconductors using a plane-wave basis set, Comput. Mater. Sci. 6 (1996) 15–50, https://doi.org/10.1016/0927-0256(96)00008-0.

[34] P.E. Blöchl, Projector augmented-wave method, Phys. Rev. B 50 (1994) 17953, https://doi.org/10.1103/PhysRevB.50.17953.

[35] G. Kresse, D. Joubert, From ultrasoft pseudopotentials to the projector augmented-wave method, Phys. Rev. B 59 (1999) 1758, https://doi.org/10.1103/PhysRevB.59.1758.

[36] J.P. Perdew, K. Burke, M. Ernzerhof, Generalized gradient approximation made simple, Phys. Rev. Lett. 77 (1996) 3865, https://doi.org/10.1103/PhysRevLett.77.3865.

[37] J.P. Perdew, K. Burke, M. Ernzerhof, Generalized gradient approximation made simple, Phys. Rev. Lett. 78 (1997) 1396, https://doi.org/10.1103/PhysRevLett.78.1396.

[38] S.H. Zhang, R.F. Zhang, AELAS: automatic ELAStic property derivations via high-throughput first-principles computation, Comput. Phys. Commun. 220 (2017) 403–416, https://doi.org/10.1016/j.cpc.2017.07.020.

[39] R. Hill, The elastic behaviour of a crystalline aggregate, Proc. Phys. Soc. 65 (1952) 349–354, https://doi.org/10.1088/0370-1298/65/5/307.

[40] G. Grimvall, Thermophysical Properties of Materials, Elsevier Science, Amsterdam, 1999.

[41] X.Q. Chen, H. Niu, D. Li, Y. Li, Modeling hardness of polycrystalline materials and bulk metallic glasses, Intermetallics 19 (2011) 1275–1281, https://doi.org/10.1016/j.intermet.2011.03.026.

[42] V.L. Moruzzi, J.F. Janak, K. Schwarz, Calculated thermal properties of metals, Phys. Rev. B 37 (1988) 790–799, https://doi.org/10.1103/PhysRevB.37.790.

[43] X.-G. Lu, M. Selleby, B. Sundman, Calculations of thermophysical properties of cubic carbides and nitrides using the Debye–Grüneisen model, Acta Mater. 55 (2007) 1215–1226, https://doi.org/10.1016/j.actamat.2006.05.054.

[44] T. Jarlborg, E.G. Moroni, G. Grimvall, α-γ transition in Ce from temperature-dependent band-structure calculations, Phys. Rev. B 55 (55) (1997) 1288–1291, https://doi.org/10.1103/PhysRevB.55.1288.

[45] C. Wolverton, A. Zunger, First-principles theory of short-range order, electronic excitations, and spin polarization in Ni-V and Pd-V alloys, Phys. Rev. B 52 (1995) 8813–8828, https://doi.org/10.1103/PhysRevB.52.8813.

[46] D.B. Miracle, O.N. Senkov, A critical review of high entropy alloys and related concepts, Acta Mater. 122 (2017) 448–511, https://doi.org/10.1016/j.actamat.2016.08.081.

[47] F. Tian, A review of solid-solution models of high-entropy alloys based on ab initio calculations, Front. Mater 4 (36) (2017), https://doi.org/10.3389/fmats.2017.00036.

[48] D. Ma, B. Grabowski, F. Körmann, J. Neugebauer, D. Raabe, Ab initio thermodynamics of the CoCrFeMnNi high entropy alloy: importance of entropy

contributions beyond the configurational one, Acta Mater. 100 (2015) 90–97, https://doi.org/10.1016/j.actamat.2015.08.050.

[49] L.-H. Li, W.-L. Wang, L. Hu, B.-B. Wei, First-principle calculations of structural, elastic and thermodynamic properties of Fe-B compounds, Intermetallics 46 (2014) 211–221, https://doi.org/10.1016/j.intermet.2013.11.007.

[50] Z. Huang, X. Lu, M. Yan, Y. Fu, Evaluating stability, elastic and thermodynamic properties of AlTiNiCuCox (x=0.5,0.75,1,1.25,1.5) high entropy alloys, Mater. Res. Express 6 (2019), https://doi.org/10.1088/2053-1591/ab48a8, 126581.

[51] X. Zhang, B. Grabowski, F. Körmann, C. Freysoldt, J. Neugebauer, Accurate electronic free energies of the 3d, 4d, and 5d transition metals at high temperatures, Phys. Rev. B 95 (2017), https://doi.org/10.1103/PhysRevB.95.165126, 165126.

[52] Y. Ikeda, B. Grabowski, F. Körmann, Ab initio phase stabilities and mechanical properties of multicomponent alloys: a comprehensive review for high entropy alloys and compositionally complex alloys, Mater. Char. 147 (2019) 464–511, https://doi.org/10.1016/j.matchar.2018.06.019.

[53] S. Wanga, D. Wub, H. Shea, M. Wua, D. Shua, et al., Design of high-ductile medium entropy alloys for dental implants, Mater. Sci. Eng. C 113 (2020) 1–7, https://doi.org/10.1016/j.msec.2020.110959.

[54] G.C. Kaschner, C.N. Tome, I.J. Beyerlein, S.C. Vogel, D.W. Brown, et al., Role of twinning in the hardening response of zirconium during temperature reloads, Acta Mater. 54/11 (2006) 2887–2896, https://doi.org/10.1016/j.actamat.2006.02.036.

[55] A.A. Salem, S.R. Kalidindi, R.D. Doherty, Strain hardening of titanium: role of deformation twinning, Acta Mater. 51 (2003) 4225–4237, https://doi.org/10.1016/S1359-6454(03)00239-8.

[56] A.A. Salem, S.R. Kalidindi, R.D. Doherty, Strain hardening regimes and microstructure evolution during large strain compression of high purity titanium, Scripta Mater. 46 (2002) 419–423, https://doi.org/10.1016/S1359-6462(02)00005-2.

[57] S.R. Kalidindi SR, A.A. Salem, R.D. Doherty, Role of deformation twinning on strain hardening in cubic and hexagonal polycrystalline metals, Adv. Eng. Mater. 5 (2003) 229–232, https://doi.org/10.1002/adem.200300320.

[58] Q. Yu, Z.W. Shan, J. Li, X. Huang, L. Xiao, et al., Strong crystal size effect on deformation twinning, Nature 463 (2010) 335–338, https://doi.org/10.1038/nature08692.

[59] G. Lütjering, J.C. Williams, Titanium, second ed., Springer, New York, 2007.

[60] J.W. Christian, S. Mahajan, Deformation twinning, Prog. Mater. Sci. 39/1 (1995) 1–157, https://doi.org/10.1016/0079-6425(94)00007-7.

[61] Y.K. Zhou, S.X. Liang, R. Jing, X.J. Jiang, M.Z. Ma, et al., Microstructure and tensile properties of hot-rolled Zr50-Ti50 binary alloy, Mater. Sci. Eng. 621 (2015) 259–262, https://doi.org/10.1016/j.msea.2014.10.079.

[62] C.M. Lin, C.C. Juan, C.H. Chang, C.W. Tsai, J.W. Yeh, Effect of Al addition on mechanical properties and microstructure of refractory AlxHfNbTaTiZr alloys, J. Alloys Compd. 624 (2015) 100–107, https://doi.org/10.1016/j.jallcom.2014.11.064.

[63] O.N. Senkov, S.V. Senkova, C. Woodward, Effect of aluminum on the microstructure and properties of two refractory high-entropy alloys, Acta Mater. 68 (2014) 214–228, https://doi.org/10.1016/j.actamat.2014.01.029.

[64] X. Yang, Y. Zhang, P.K. Liaw, Microstructure and compressive properties of NbTiVTaAlx high entropy alloys, Process Eng. 36 (2012) 292–298, https://doi.org/10.1016/j.proeng.2012.03.043.

[65] N.Y. Yurchenko, N.D. Stepanov, D.G. Shaysultanov, M.A. Tikhonovsky, G. A. Salishchev, Effect of Al content on structure and mechanical properties of the AlxCrNbTiVZr (x=0; 0.25; 0.5; 1) high-entropy alloys, Mater. Char. 121 (2016) 125–134, https://doi.org/10.1016/j.matchar.2016.09.039.

[66] M. Abdel-Hady, K. Hinoshita, M. Morinaga, General approach to phase stability and elastic properties of β-type Ti-alloys using electronic parameters, Scripta Mater. 5 (/5) (2006) 477–480, https://doi.org/10.1016/j.scriptamat.2006.04.022.

[67] L. Lilensten, J.-P. Couzinié, J. Bourgon, L. Perrière, G. Dirras, F. Prima, I. Guillot, Design and tensile properties of a bcc Ti-rich high-entropy alloy with transformation-induced plasticity, Materials Research Letters 5 (2) (2017) 110–116, https://doi.org/10.1080/21663831.2016.1221861.

[68] S. Zherebtsov, N. Yurchenko, E. Panina, A. Tojibaev, M. Tikhonovsky, G. Salishchev, N. Stepanov, Microband-induced plasticity in a Ti-rich high-entropy alloy, J. Alloys Compd. 842/25 (2020) 155868, https://doi.org/10.1016/j.jallcom.2020.155868.

[69] R.R. Eleti, M. Klimova, M. Tikhonovsky, et al., Exceptionally high strain-hardening and ductility due to transformation induced plasticity effect in Ti-rich high-entropy alloys, Sci. Rep. 10 (2020) 13293, https://doi.org/10.1038/s41598-020-70298-2.

[70] Liang Wang, Tangqing Cao, Xudong Liu, Benpeng Wang, A novel stress-induced martensitic transformation in a single-phase refractory high-entropy alloy, Scripta Mater. 189 (2020) 129–134, https://doi.org/10.1016/j.scriptamat.2020.08.013.

[71] J. Haines, J.M. Leger, G. Bocquillon, Synthesis and design of superhard materials, Annu. Rev. Mater. Res. 31 (2001) 1–23, https://doi.org/10.1146/annurev.matsci.31.1.1.